Extracting High-Level Intuitive Features (HLIF) For Classifying Skin Lesions Using Standard Camera Images

Robert Amelard, Alexander Wong, David A. Clausi
Vision and Image Processing (VIP) Research Group
Department of Systems Design Engineering
University of Waterloo, Waterloo, Canada
{*ramelard,a28wong,dclausi*}*@uwaterloo.ca*

***Abstract*—High-level intuitive features (HLIF) that measure asymmetry of skin lesion images obtained using standard cameras are presented. These features can be used to help dermatologists objectively diagnose lesions as cancerous (melanoma) or benign with intuitive rationale. Existing work defines large sets of low-level statistical features for analysing skin lesions. The proposed HLIFs are designed such that smaller sets of HLIFs can capture more deterministic information than large sets of low-level features. Analytical reasoning is given for each feature to show how it aptly describes asymmetry. Promising experimental results show that classification using the proposed HLIF set, although only one-half the size of the existing state-of-the-art low-level asymmetry feature subset, labels the data with better success. The best classification is obtained by combining the low-level feature set with the HLIF set.**

***Keywords*-feature extraction, feature descriptor, melanoma, skin lesion, decision support**

I. Introduction

Melanoma is the leading cause of death from all skin diseases [1]. The World Health Organization (WHO) estimates that one third of all cancer cases are skin cancers; there are currently 132,000 new melanoma cases each year worldwide; and one in five Americans is expected to develop malignant melanoma in their lifetime [4]. Furthermore, the WHO indicates that the ozone depletion is affecting this number, and that every 10 percent decrease in ozone levels will result in an additional 4,500 melanoma cases globally. Early detection of melanoma is pivotal to the patient's prognosis. The five-year survival rate of patients whose melanoma is caught early is 98%, whereas the survival rate is 62% for cases of melanoma that have spread beyond the regional tissue, and a dismal 16% survival rate for cases of melanoma that have spread to parts of the body remote from the primary tumour [5].

To date, the majority of dermatologists diagnose a lesion by performing a type of manual pattern recognition based on their prior knowledge of malignant and benign cases. This leads to a very subjective and qualitative diagnosis. It also takes years of experience for a doctor to become adept at classifying lesions with an acceptable degree of accuracy [7]. One of the most common diagnostic rubrics is the "ABCD" rubric [2], [3], whereby the dermatologist looks for patterns of asymmetry (A) about the lesion, border irregularity (B), colour variation (C), and a large diameter (D). It has been reported that expert dermatologists achieve on average only 82.6% sensitivity (i.e., correctly identified malignant cases) and 70% specificity (i.e., correctly identified benign cases) in their diagnosis of melanoma using dermatoscopes [6].

Prior work on automated melanoma detection has been mostly limited to the analysis of dermoscopic images [9]–[16]. These images are obtained using a digital dermatoscope, which is a specialized tool that provides a magnified images of detailed pigment structures without any skin surface reflection. Application of these techniques are limited, since hospitals do not readily have dermatoscopes that can store digital images. In fact, it has been reported that only 48% of practicing dermatologists in the USA use a dermatoscope in their diagnosis [8]. Furthermore, it restricts the application to hospital settings only.

There have been some recent developments using standard camera images for melanoma detection [17], [18]. However, these papers have focused primarily on the preprocessing step of melanoma detection (i.e., illumination standardization), and have simply incorporated a large feature set that loosely describes ABCD without analytical justification for their decision. In practice, a high dimensional feature space may decrease the classifier's ability to generalise to new data, since there is no learning algorithm that can account for all of the variability of the data, and thus the classifier will tend to overfit the (sparse) training data [20]. It should also be noted that melanoma data sets are not very common, and a large feature space can easily lead to overfitting due to this curse of dimensionality.

The main contribution of this paper is the analytical identification and extraction of a set of high-level intuitive features (HLIF) that quantitatively describe a lesion's asymmetry. We define "high-level intuitive" features as features that have been designed to describe an understandable qualitative phenomenon (e.g., amount of asymmetry of a shape), and whose score can be intuitively interpreted. This is in contrast to low-level features, which are generic calculations that were not designed with a specific high-level description in mind (e.g., solidity and equivalent diameter). Building

intuitive features allows the system to be queried for the reasoning behind a diagnosis, which is important if doctors are to trust and analyse the system's choices. Unlike in previous work where features were stated without rationale [17], [18], rigid analytical reasoning of the features is given.

We measure success according to sensitivity, specificity, accuracy, and leave-one-out cross-validation error using a support vector machine (SVM) classifier [19]. The proposed features are concatenated to a slightly modified version of Cavalcanti *et al.*'s feature set [18] to produce a new 54-dimensional feature space. The performance of this new set is compared against the performance of their original set on the same data. Note that feature extraction and classification is done using manually-defined segmentations. Automated lesion segmentation is a separate problem not addressed here.

This paper is organized as follows. The proposed features are presented in Section II. The experimental results including a comparison with the state-of-the-art method is presented in Section III. Conclusions are drawn and future work is discussed in Section IV.

II. Feature Extraction

As mentioned previously, dermatologists employ the ABCD rubric in a very qualitative and subjective manner that leads to large inter-observer bias as well as some intra-observer bias [7]. To provide a more quantitative and objective basis for melanoma detection, HLIFs that represent the asymmetry characteristic of the ABCD rubric are extracted from lesion images. The classification of lesions with respect to these features provides strict numerically-driven reasoning behind diagnosis decisions, which we hope will increase doctors' sensitivity and specificity metrics. It can also shorten the large accuracy gap between new and seasoned doctors by providing the new doctors with information describing features of interest. The feature scores can also be transformed into a qualitative (yet still objective) measure simply by mapping the score relative to the mean and standard deviation of the score distribution to a qualitative class (e.g., "Very Asymmetric", "Very Symmetric", etc.).

A. Clinical Asymmetry Description

In general, lesions are described as asymmetric with respect to colour and shape about an axis. Clinically, the asymmetry of a lesion is measured along two orthogonal axes chosen by the dermatologist [3]. The asymmetry score is then determined by giving a binary score of 1 for "asymmetric" and 0 otherwise for each axis. The scores for both axes are then summed, giving $A \in \{0, 1, 2\}$. This set of scores is not only very restricted, but the actual scores themselves are determined subjectively. We take a more precise approach by evaluating strict numerical models of structural and colour variation of the lesion in its entirety.

B. HLIF for Colour Asymmetry

Asymmetry with respect to colour can be characterized by separating the lesion along a set of axes that pass through the centroid of the lesion, and then comparing the normalized hue histograms of both partitions.

First, we calculated the major axis of the lesion that has the same second-order central moments as the lesion shape. This axis passes through the centroid and separates the image into two partitions along the axis that describes the maximum variance of the lesion. The image was converted to the Hue-Saturation-Value (HSV) domain, and the normalized hue histogram was computed for each partition. Thus, the histogram represents the probability density function of the hue space. The histograms were shifted such that the beginning and end of the x-axis represent green hues, which are rarely seen in skin lesions thus minimising any chance of discontinuity. These histograms were subsequently smoothed using a Gaussian filter so that we could compare histograms of approximate hues rather than discrete hue values for robustness. We found that using $\sigma = 0.5$ (i.e., half a bin) resulted in a good estimate of the local hue information while still maintaining the general structure of the original distribution. We used 256 bins. This calculation was repeated for many axes of separation by rotating the major axis by $\frac{\pi}{n}$ radians $(n-1)$ times, where n is the number of separation axes. We used $n = 16$.

The HLIF was then defined as the maximum sum of absolute differences of the smoothed histograms with respect to the rotation angle:

$$f_1^A = \max_{\theta} \left\{ \frac{1}{2} \sum_{i=1}^{nbins} |H_1^\theta(i) - H_2^\theta(i)| \right\} \tag{1}$$

where H_1^θ and H_2^θ are the normalized, smoothed histograms described above for the separation axis defined by rotating the major axis by θ, and $nbins$ is the number of hue bins. The result was divided by 2 to normalize it such that $f_1^A \in [0, 1]$, since $\forall k, \sum_{i=1}^{nbins} H_k^\theta(i) = 1$. This score can be intuitively interpreted as the maximum amount of colour asymmetry on a scale from 0 (completely symmetric) to 1 (completely asymmetric).

Fig. 1 depicts an example of this feature calculation. The θ value that produced the maximum asymmetry value was found. The resulting separation axis and corresponding normalized histograms are shown. The apparent colour asymmetry of the lesion is reflected in these histograms such that Fig. 1b shows the abundance of red hues present on the left side of the axis, whereas Fig. 1c shows the distribution of both red and blue hues on the right side of the axis.

C. HLIF for Structural Asymmetry

1) HLIF for Irregular Shapes: Structurally asymmetric lesions have irregular oblong shapes. Fourier descriptors

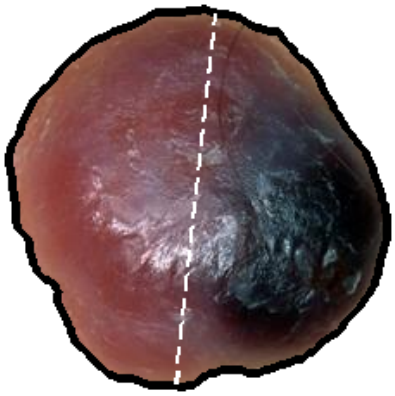

(a) Image of the segmented skin lesion. The dashed white line represents the axis of separation that produces maximal colour asymmetry.

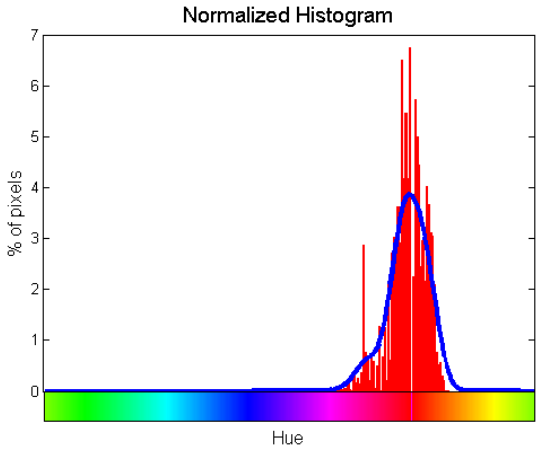

(b) Normalized histogram of the left side of the lesion. Note the high concentration of red hues.

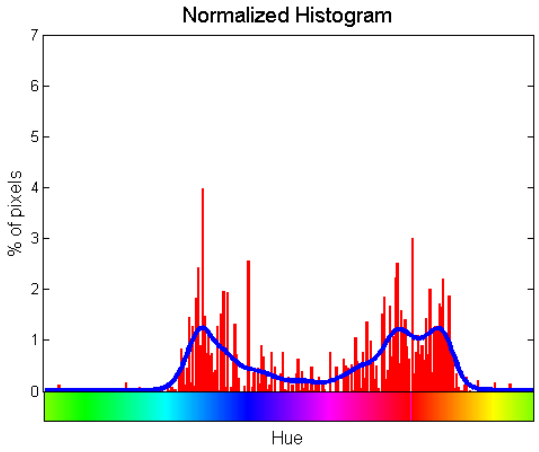

(c) Normalized histogram of the right side of the lesion. Note the concentration of both blue and red hues.

Figure 1. Comparing the normalized histograms of two partitions of a lesion diagnosed as malignant melanoma (nodular melanoma). The red bars represent the concentration of each hue value, whereas the blue curves represent the Gaussian smoothed version of the histogram ($\sigma = 0.5$). This allows us to compare approximate colours rather than discrete hue values. In this example, $f_1^A = 0.5300$, indicating a large portion of colour asymmetry.

are used to describe a shape in terms of constituent frequency bands. Determining a shape's Fourier descriptors is accomplished by representing the x-axis as the real axis, and the y-axis as the imaginary axis. Thus the points of the shape border are transformed into a 1D complex number. In particular $F : (x, y) \mapsto x + \imath y$. Given this representation, a Fourier transform can decompose it into its constituent sinusoidal waves. Hence, a reconstruction of the lesion shape using only low frequency Fourier descriptors will produce a rough estimate of the original shape. This rough estimate can be compared with its full representation to detect oblong parts of the lesion.

First the lesion border is sampled by a pre-determined rate so that the frequency resolution is fixed across all lesions irrespective of their perimeter length. Upon computing the Fast Fourier Transform (FFT) of the lesion's sampled perimeter, a coarse representation was reconstructed using only the two lowest frequency components. These frequencies represent the zero-frequency mean as well as the most basic components needed to construct the general shape of the lesion. It was empirically found that reconstruction with more than two frequencies produced a shape that incorporated too much variability. It is apparent that a lesion with a highly irregular shape will have a more varying perimeter than the low-frequency representation of that same lesion. However, comparing the two-frequency reconstruction with the original border will produce skewed results, as a lesion with a highly irregular border would result in a high feature score (this would be a feature more suitable for detecting border irregularity). Thus, the shape of the resulting two-frequency representation was compared to the shape of another low-frequency representation to yield the HLIF:

$$f_2^A = \frac{area(S_{low} \oplus S_2)}{area(S_{low} \cup S_2)} \tag{2}$$

where S_{low} and S_2 are the low-frequency and two-frequency reconstruction, and $S_{low} \cup S_2$ is the union of these two reconstructions. This score can be intuitively interpreted as the amount of general structural variation of a lesion's border. We found that sampling the border with 1000 points and reconstructing the shape of the lesion using five frequency components yielded a good approximate shape that incorporated the structural variations.

Fig. 2 depicts an example of this feature calculation. The lesion has a very irregular shape with many peaks and valleys. Notice the difference between the shape of the two-frequency reconstruction (pink), which gives only the general shape of the lesion border, and the five-frequency reconstruction (cyan), which reflects the variability due to the irregularly curvy parts. This difference was coloured in with black for visualization purposes.

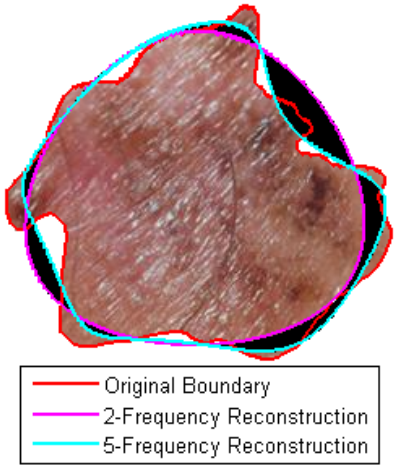

Figure 2. Depiction of an asymmetric lesion diagnosed as malignant melanoma (lentigo maligna melanoma). The difference of the two reconstructions was coloured black for visualization purposes. Note how the two-frequency reconstruction (pink) of the original boundary captures only the very general shape of the lesion, whereas the five-frequency reconstruction (cyan) captures more of the irregular variability. In this example, $f_2^A = 0.1199$, indicating the presence of structural variation.

2) HLIF for Asymmetric Areas: Cavalcanti *et al.* [18] propose the following 4 HLIFs:

- f_8: $(B_1 - B_2)/A$ with respect to L_1,
- f_9: $(B_1 - B_2)/A$ with respect to L_2,
- f_{10}: B_1/B_2 with respect to L_1,
- f_{11}: B_1/B_2 with respect to L_2

where L_1 and L_2 are the orthogonal major and minor axes, and B_1 and B_2 are the areas to each side of the axis. Fig. 3 shows an example of separating a shape along its major and minor axes with the resulting areas coloured for visualization purposes. Note that these definitions do not put any constraints on the relative sizes of B_1 and B_2. Thus, depending on the order of the areas, f_8 and f_9 can result in either a positive or negative value, and f_{10} and f_{11} can result in either a large or small value. So, for the sake of clarity we propose to extend these HLIFs in the following way:

Figure 3. Depiction of an asymmetric lesion diagnosed as malignant melanoma (superficial spreading melanoma). The red and green areas indicate the two partitions about the major and minor axes. Note the difference in areas about the minor axis due primarily to the tail-like structure in the red area, indicating an asymmetric lesion. In this example, $f_3^A = 0.2067$, $f_4^A = 0.2656$, $f_5^A = 0.5211$, $f_6^A = 0.7234$, indicating some asymmetry about the major axis and lots of structural asymmetry about the minor axis.

$$f_3^A = (A_1 - A_2)/A \text{ with respect to } L_1, \quad (3)$$
$$f_4^A = (A_1 - A_2)/A \text{ with respect to } L_2, \quad (4)$$
$$f_5^A = (A_1 - A_2)/A_2 \text{ with respect to } L_1, \quad (5)$$
$$f_6^A = (A_1 - A_2)/A_2 \text{ with respect to } L_2 \quad (6)$$

such that the following constraints are satisfied:

$$A_1 = \max\{B_1, B_2\},$$
$$A_2 = \min\{B_1, B_2\}$$

where B_1 and B_2 are the areas on each side of the axis. Thus, $\{f_3^A, f_4^A\}$ represent the positive difference between the two areas as a percentage of the total area, and $\{f_5^A, f_6^A\}$ represent the same difference as a percentage of the smaller area. By this definition, asymmetric lesions will have larger values for $\{f_3^A, f_4^A, f_5^A, f_6^A\}$ than symmetric lesions. Intuitively, f_3^A and f_4^A represent the amount of structural difference about the major and minor axis respectively relative to the entire area. Similarly, f_5^A and f_6^A represent the structural difference of the larger side of the major/minor axis relative to the smaller area. Fig. 3 depicts an example of a lesion that has been separated by its major and minor axes. Note that the difference in areas (shown in red and green for visualization purposes) captures the asymmetry about the axis.

III. Experimental Results

Our data set comprises 206 images; 69 from the Dermatology Information System [21] (43 malignant melanomas and 26 nevi), and 137 from DermQuest [22] (76 malignant melanomas and 61 nevi). The data set includes images of the 6 major types of melanoma, as well as various typical nevi including many dysplastic nevi. Each image contains only a single lesion. These images were manually segmented to construct the binary lesion mask. For the proposed HLIFs, the images were rotated such that the major axis aligned with the horizontal for rotation invariance. The lesion was then scaled such that its bounding box fit in a 200×200 pixel

Table I
COMPARING CLASSIFICATION RESULTS OF DIFFERENT FEATURE SETS. LOO CV IS "LEAVE-ONE-OUT CROSS-VALIDATION".

Feature set	Description (see Section III)	# features	Sensitivity	Specificity	Accuracy	LOO CV Error
F_C^A	Asymmetry features from F_C	11	73.11%	64.37%	69.42%	30.58%
F_{HLIF}^A	Proposed asymmetry HLIFs	6	**79.83%**	**68.97%**	**75.24%**	**24.76%**
F_C	Cavalcanti *et al.* feature set [18]	52	84.87%	78.16%	82.04%	17.96%
F_{CM}	Modified F_C (see Section II-C2)	48	86.55%	75.86%	82.04%	17.96%
F_T	Combined F_{CM} and F_{HLIF}^A	54	**91.60%**	**80.46%**	**86.89%**	**13.11%**

box while preserving its aspect ratio. The images underwent Cavalcanti *et al.*'s illumination invariance algorithm prior to feature extraction. All images were obtained using standard cameras. Fig. 4 shows some typical sample data from our data set. Due to the small size of the data set, standard leave-one-out cross-validation (LOO CV) error was used to compute the test error. Sensitivity, specificity, and accuracy were also computed as success metrics.

For clarity, we use the following notation to refer to the various feature sets throughout this section:

- $\boldsymbol{F_{HLIF}^A}$: feature set containing the 6 proposed HLIFs describing asymmetry (see Section II).
- $\boldsymbol{F_C}$: feature set containing Cavalcanti *et al.*'s 52 low-level features describing asymmetry, border irregularity, colour variation, and differential structures [18].
- $\boldsymbol{F_C^A}$: subset of F_C containing only their asymmetry features ($F_C^A \subset F_C$).
- $\boldsymbol{F_{CM}}$: a modified version of the set F_C without the four features identified in Section II-C2 ($F_{CM} = F_C \backslash \{f_8, \ldots, f_{11}\} \subset F_C$).
- $\boldsymbol{F_T}$: the "total" superset containing the features from the proposed F_{HLIF}^A and F_C ($F_T = F_{CM} \cup F_{HLIF}^A$).

The extraction of F_{HLIF}^A and F_C was implemented in MATLAB. F_C is comprised of 52 features categorized as follows: 11 features for asymmetry, 12 features for border irregularity, 25 features for colour variation, and 4 features for differential structures [18]. The combined feature set F_T resulted in a 54-dimensional feature space.

We evaluated the feature sets in the following ways. First we normalized the data by centering the data points at their mean and scaling them to have a unit standard deviation. We then used SVM without a kernel to classify the data set, setting the soft margin parameter to minimize LOO CV error. We chose to use the standard SVM model so that the classification results strictly reflect the linear separability of the data, rather than the performance of the classifier. In general, the goal of extracting features is to represent the data in a feature space such that it is easy to distinguish one class from another. SVM is regarded as one of the most robust classifiers, and does not tend to overfit (as opposed to, for example, nearest neighbour). Due to the small size of the data set, this is an important characteristic.

We then compared the experimental results of F_{HLIF}^A against the asymmetry features from F_C (denoted F_C^A), F_C, F_{CM}, and F_T on the same data. In particular, we calculated the sensitivity, specificity, accuracy, and the LOO CV error of the SVM classification using each of the feature sets. The classification results of the various feature sets are summarized in Table I.

A. Classification Using Asymmetry Features

Classification using F_{HLIF}^A was compared against classification using only the asymmetry features from Cavalcanti *et al.*'s feature set, F_C^A. It is not surprising that F_C^A performs inadequately as a melanoma detection feature set on its own (73.11% sensitivity, 64.37% specificity, 69.42% accuracy, 30.58% LOO CV error), since the set contains only low-level features that describe asymmetry. Low-level feature sets depend on a large number of features to represent detailed data. In comparison, F_{HLIF}^A, which itself only defines asymmetry features as well, performs better with respect to classifying the entire data set (79.83% sensitivity, 68.97% specificity, 75.24% accuracy, 24.76% LOO CV error). Furthermore, F_{HLIF}^A only defines 6 features, whereas F_C^A defines 11 features. These results indicate that asymmetry is a very important characteristic when analysing skin lesions, and HLIFs that describe a lesion's asymmetry captures a lot of the underlying data in an intuitive manner. This shows the power of HLIFs as a means of quantitatively describing data.

B. Classification Using All ABCD Features

As expected, classification using the smaller set F_{CM} performs comparably to its superset F_C in terms of sensitivity, specificity, accuracy, and LOO CV error. We therefore use this reduced feature set as the benchmark in the analysis below.

Although the classification of F_{CM} attains high sensitivity and specificity measures on the data set, it must be noted that the data is projected into 48 dimensions. It is usually easy to find many hyperplanes that perfectly separate data in some high dimensional space, where the number of dimensions is close to the number of data points [20]. The presence of a high LOO CV error (17.96%) shows that this is indeed the case with this data set; that is, the feature space does not generalize well to new data. In their paper, Cavalcanti

(a) Lentigo Maligna Melanoma (b) Nodular Melanoma (c) Superficial Spreading Melanoma

(d) Blue Nevus (e) Dysplastic Nevus (f) Dysplastic Nevus

Figure 4. Sample data from the data set. The manually segmented lesion border has been superimposed on the image for visualization purposes.

et al. attempt to circumvent this problem by using the Smoothed Bootstrap Resampling method to generate new data. However, this method simply introduces some zero-mean noise to the original data set, and is thus not a good representation of skin lesion images, as each patient case can be very different from another.

Another noteworthy observation is the fact that F_T attains very high success metrics (91.60% sensitivity, 80.46% specificity, and 86.89% accuracy, with a 13.11% LOO CV error). The low cross-validation error is important since overfitting is very possible with such a high dimensional feature space (i.e., 54 dimensions). This combined feature set attains almost 30% less cross-validation error than F_{CM} (17.96% and 13.11% respectively), indicating that the addition of the HLIFs to F_{CM} results in a much more descriptive and interpretive model.

C. Sources of Error

Examples of where the classification using F_T performed well and where it performed poorly are given in Fig. 5. There is a high saturation of white pixels in the first image due to the flash of the camera. This drastically skewed the results of the histogram comparison, f_1^A, as well as the Cavalcanti *et al.*'s gradient measures. The other false negative cases have very irregular borders, indicating that there is a need for HLIFs describing border irregularity.

Most of the false positive cases exhibit a very distinct colour variation, thus resembling a malignant melanoma. In particular, it can be noted that there is a high concentration of dark cells in 3 of the 4 presented images. Further investigation should try to distinguish the difference between these pigmented concentrations in benign versus malignant case to separate this kind of data.

IV. Conclusion

In this paper we have proposed a set of HLIFs for describing the amount of asymmetry of a skin lesion image obtained from a standard camera to help diagnose it as melanoma or not melanoma. Designing HLIFs allows the system to represent its diagnosis in terms of objective, understandable steps both quantitatively (i.e., raw feature score) and qualitatively (i.e., description of the feature score). Furthermore, it simplifies the feature selection process, as each HLIF is designed according to human interpretation of the data. Experimental results indicate that the small proposed HLIF set of asymmetry features alone attains better sensitivity, specificity, and accuracy as Cavalcanti *et al.*'s large low-level asymmetry feature set, while exhibiting a lower cross-validation error using a simple linear SVM model. Furthermore, adding the proposed HLIF set to a slightly modified version of Cavalcanti *et al.*'s entire feature set gives drastically improved success metrics over their original set. Future work involves designing HLIFs to describe a lesion's border irregularity and colour variation.

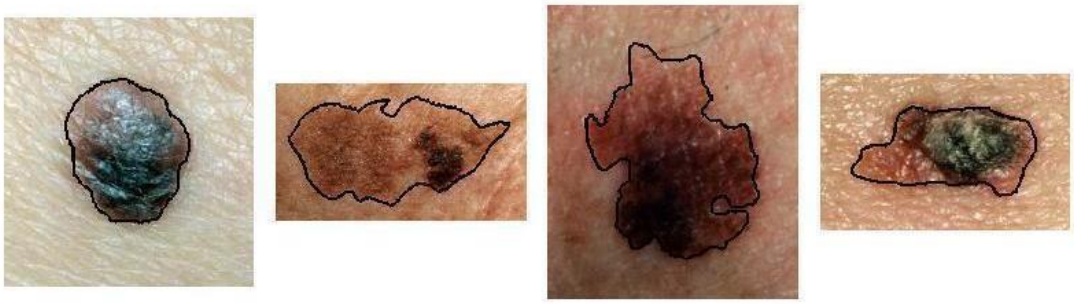

(a) False Negatives

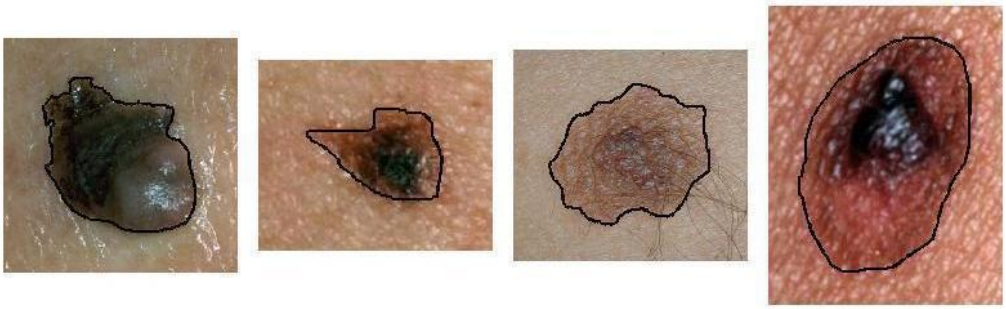

(b) False Positives

Figure 5. Examples of images that were misclassified. The manually segmented lesion border has been superimposed on the image for visualization purposes.

Also, a more thorough analysis of the HLIF set's feature space and the resulting data clusters will be conducted with a larger data set.

ACKNOWLEDGMENT

This research was sponsored by Agfa Healthcare Inc., Ontario Centres of Excellence (OCE), and the Natural Sciences and Engineering Research Council (NSERC) of Canada.

REFERENCES

[1] *Melanoma – PubMed Health*, U.S. National Library of Medicine [Online]. Available: http://www.ncbi.nlm.nih.gov/pubmedhealth/PMH0001853

[2] W. Stolz *et al.*, "ABCD rule of dermatoscopy: a new practical method for early recognition of malignant melanoma," *European J. of Dermatology*, vol. 4, pp. 521-527, 1994.

[3] F. Nachbar *et al.*, "The ABCD rule of dermatoscopy: high prospective value in the diagnosis of doubtful melanocytic skin lesions," *J. of the Amer. Academy of Dermatology*, vol. 30, no. 4, pp. 551-559, Apr. 1994.

[4] *WHO | Skin cancers*, World Health Organization [Online]. Available: http://www.who.int/uv/faq/skincancer/en/index1.html

[5] "Cancer Facts & Figures 2011," American Cancer Society, Atlanta, GA, Tech. Rep. ACSPC-029771, 2011.

[6] C. A. Morton, R. M. Mackie, "Clinical accuracy of the diagnosis of cutaneous malignant melanoma," *British J. of Dermatology*, vol. 138, no. 2, pp. 283-287, Feb. 1998.

[7] G. Argenziano *et al.*, "Dermoscopy of pigmented skin lesions: Results of a consensus meeting via the Internet," *J. of Amer. Academy of Dermatology*, vol. 48, no. 5, pp. 679-693, May 2003.

[8] H. C. Engasser, E. M. Warshaw, "Dermatoscopy use by US dermatologists: A cross-sectional survey," *J. of Amer. Academy of Dermatology*, vol. 63, no. 3, pp. 412-419, Sep. 2010.

[9] H. Iyatomi *et al.*, "Classification of melanocytic skin lesions from non-melanocytic lesions," in *Engineering in Medicine and Biology Society (EMBC), 2010 Ann. Int. Conf. of the IEEE*, Buenos Aires, Argentina, 2010, pp. 5407-5410.

[10] Q. Abbas *et al.*, "Computer-aided pattern classification system for dermoscopy images," in *Skin Research and Technology*, Aug. 2011. doi: 10.1111/j.1600-0846.2011.00562.x

[11] B. Shrestha *et al.*, "Detection of atypical texture features in early malignant melanoma," *Skin Research and Technology*, vol. 16, no. 1, pp. 60-65, Feb. 2010.

[12] G. Capdehourat *et al.*, "Pigmented skin lesions classification using dermatoscopic images," *Progress in Pattern Recognition, Image Anal., Comput. Vision, and Applicat.*, vol. 5856, pp. 537-544, 2009.

[13] M. E. Celebi *et al.*, "A methodological approach to the classification of dermoscopy images," *Computerized Medical Imaging and Graph.*, vol. 31, pp. 362-373, Sep. 2007.

[14] T. K. Lee *et al.*, "Describing the structural shape of melanocytic lesions," in *Proc. SPIE 3661, Medical Imaging*, 1999, vol. 3661, pp. 1170-1179.

[15] M. Elbaum, "Computer-aided melanoma diagnosis," *Dermatologic Clinics*, vol. 20, no. 4, pp. 1-6, Oct. 2002.

[16] L. Xu *et al.*, "Segmentation of skin cancer images," *Image Vision and Computing*, vol. 17, pp. 65-74, Jan. 1999.

[17] J. F. Alcon *et al.*, "Automatic imaging system with decision support for inspection of pigmented skin lesions and melanoma diagnosis," *IEEE J. of Sel. Topics Signal Process.*, vol. 3, no. 1, Feb. 2009.

[18] P. G. Cavalcanti, J. Scharcanski, "Automated prescreening of pigmented skin lesions using standard cameras," *Computerized Medical Imaging and Graph.*, vol. 35, no. 6, pp. 481-491, Sep. 2011.

[19] C. Cortes, V. Vapnik, "Support-vector networks," *Machine Learning*, vol. 20, no. 3, pp. 273-297, Sep. 1995.

[20] G. Hughes, "On the mean accuracy of statistical pattern recognizers," *IEEE Trans. on Information Theory*, vol. 14, no. 1, pp. 55-63, Jan. 1968.

[21] *DermIS* [Online]. Available: http://www.dermis.net

[22] *DermQuest* [Online]. Available: http://www.dermquest.com